Quantifying the Dynamic Evolution of Graded Gravel Beds Using Particle Tracking Velocimetry

K. G. Heays[1]; H. Friedrich[2]; B. W. Melville, M.ASCE[3]; and R. Nokes[4]

Abstract: The motion of graded gravels under steady and spatially uniform turbulent flow is investigated in laboratory conditions using particle tracking velocimetry (PTV). The gravel bed is subjected to flows approaching critical armor velocity, and water worked until static armor is reached. A digital particle tracking (DPT) algorithm, based on image subtraction between subsequent frames, is developed and applied on the particle scale as the graded gravel bed is water-worked. The dynamic evolution of graded gravels is quantified continuously for up to 8 h. Characteristics of particle motion are identified, and movement patterns under complex flow conditions are analyzed. Particle tracking is applied to low-frequency (0.67-fps) and high-frequency (30-fps) data. This study provides a new perspective on gravel particle transport distances, trajectory sinuosity, sediment transport rate, fractional sediment transport rates, particle movement patterns, and instantaneous particle velocities. **DOI:** **10.1061/(ASCE)HY.1943-7900.0000850.** © *2014 American Society of Civil Engineers.*

Author keywords: Digital particle tracking (DPT); Sediment transport; Image analysis; Graded gravel.

Introduction

Bedload motion refers to the transport of streambed particles in a rolling, sliding, or saltating motion; it is the dominant form of sediment transport in gravel-bed rivers. The entrainment and transport of bedload is the fundamental process in the formation of bedforms and ultimately river morphodynamics. The understanding of river morphology is of particular importance in both engineering and ecological applications, such as local scour, river incising, stable channel design, siltation of reservoirs, and aquatic habitat (Biggs et al. 1997; Yalin 1977; Yalin and DaSilva 2001). Major advances in the investigation of sediment motion under water flow have been made in the past three decades as technology has allowed increasingly sophisticated measurement of fluid and sediment dynamics (Drake et al. 1988; Hergault et al. 2010; Lajeunesse et al. 2010; Papanicolaou et al. 1999).

Sediment entrainment is a complex process. The role of near-bed turbulence has been identified as a major influence on the stochastic nature of sediment entrainment at the grain scale. Within a turbulence event, sweeps and ejections, which both contribute positively to the mean bed shear stress, commonly have been identified as the dominant phenomena responsible for particle mobilization (Dwivedi et al. 2010; Grass 1971). Further studies have identified that sediment entrainment is also highly correlated to streamwise velocity fluctuations, termed *outward interactions* (Nelson et al. 1995; Papanicolaou 1997; Wu and Yang 2004). In addition to those near-bed turbulence effects, sediment entrainment is influenced by bed geometry, which introduces intergranular geometric influences such as the formation of secondary flow cells around larger particles, grain protrusion effects, and friction angle effects (Buffington et al. 1992; Chin 1985; Wu and Yang 2004). Graded sediment is inherently subject to these added complexities (Komar 1987; Parker and Klingeman 1982), which is reflected in an observed reduction in bedload transport rates of natural gravel streams compared to the rates predicted by existing bedload transport formulas (Bathurst 2007; Buffington and Montgomery 1997; Wilcock 2001).

The use of image analysis in the study of bedload motion was first highlighted by the observations on individual and collective particle movements by Drake et al. (1988). However, this work also highlighted the need for automated processing of images to avoid time-consuming manual processing. Since then, a number of studies have used image analysis, and significant progress has been made in the detection of particle motion (Heays et al. 2010; Keshavarzy and Ball 1999; Lane et al. 2001; Radice et al. 2006; Schuyler and Papanicolaou 2000).

The challenge in the isolation and identification of a discrete particle arises from the lack of contrast between the particle and the background. Contrast has been achieved by a number of researchers using various techniques. Examples include using a plate directly downstream of the sediment entrainment area, providing contrast to particles as they pass (Radice et al. 2006, 2010; Zimmermann et al. 2008), using artificial particles and a fixed bed of contrasting color (Schuyler and Papanicolaou 2000), using color to differentiate between particles (Hassan and Church 2000; Houssais and Lajeunesse 2012; Lajeunesse et al. 2010; Wilcock and McArdell 1993) and observing particles from the side in a narrow flume, which allows the observation of only one grain width (Böhm et al. 2004, 2006; Hergault et al. 2010).

An additional challenge in capturing particle movements is the detection of particle pathlines. Using an approach similar to particle tracking velocimetry (PTV) algorithms, Böhm et al. (2006) successfully tracked two-dimensional motion of spherical glass particles from the side of the flume. PTV uses the previous known

[1]Dept. of Civil and Environmental Engineering, Univ. of Auckland, 20 Symonds St., Auckland 1010, New Zealand (corresponding author). E-mail: kheays@tonkin.co.nz

[2]Lecturer, Dept. of Civil and Environmental Engineering, Univ. of Auckland, 20 Symonds St., Auckland 1010, New Zealand. E-mail: h.friedrich@auckland.ac.nz

[3]Professor, Dept. of Civil and Environmental Engineering, Univ. of Auckland, 20 Symonds St., Auckland 1010, New Zealand. E-mail: b.melville@auckland.ac.nz

[4]Professor, Dept. of Civil and Natural Resources Engineering, Univ. of Canterbury, Christchurch 8140, New Zealand. E-mail: roger.nokes@canterbury.ac.nz

Note. This manuscript was submitted on March 20, 2013; approved on December 4, 2013; published online on March 18, 2014. Discussion period open until August 18, 2014; separate discussions must be submitted for individual papers. This paper is part of the ***Journal of Hydraulic Engineering***, © ASCE, ISSN 0733-9429/04014027(9)/$25.00.

positions of a particle to predict the trajectory. Böhm et al. (2006) reported that distinguishing particles over time was critically dependent on the displacement of the particle being less than the particle diameter between consecutive images. This algorithm since has been applied to two sizes of glass beads, and was used to track the movement of every visible bead in view rather than the common approach of tracking only those particles that are moving (Ancey et al. 2008; Böhm et al. 2004, 2006; Hergault et al. 2010). The ease of capturing sediment movement when observing from above is strongly dictated by the number of particles that are in motion on the bed surface. Particle image velocimetry (PIV) has been applied to measure the concentration and regional particle velocity of moving grains (Keshavarzy and Ball 1999; Radice et al. 2006). Although this method is well suited to applications on multiple moving grains, it does not allow the detection of individual particle movements.

While studying artificial gravel beds with PTV, Radice et al. (2010) recognized that the application of PTV to the detection of sediment motion was challenged by the frequent starts and stops of sediment and inconsistent particle trajectories. Other studies have successfully developed algorithms for tracking particles; Papanicolaou et al. (1999) developed a particle tracking algorithm to track colored glass beads on a fixed bed, and Pilotti et al. (1997) used an overhead linear camera, which photographed a single line of pixels, to record the passing of grains on the bed below. Houssais and Lajeunesse (2012) and Lajeunesse et al. (2010) used PTV to determine the trajectories of quartz grains in a moveable bed. In those studies, a small fraction of the grains were colored, allowing the tracking of a reduced number of grains.

Objective

To the authors' knowledge, previous particle tracking studies have been applied in experimental conditions that were simplified by using idealized particles and fixed beds, tracking small fractions of the total bed, or using short experimental run times. Thus, the aim of this study was to investigate gravel-bed dynamics over a long period of time with PTV, maintaining a high level of detail in measurement and setting up a physical model capable of mimicking complex natural processes, such as the evolution of cluster formations. The newly developed digital particle tracking (DPT) algorithm used for this study is introduced in detail. It allowed for analyzing graded gravel bed motion on the particle scale in the high-frequency domain, as well as over extended time periods. The characteristics of particle motion on a graded gravel bed are quantified, and movement patterns under complex flow conditions are detected and presented.

Experimental Setup and Testing

Experimental Conditions

Experiments were conducted in the Hydraulics Laboratory at the University of Auckland. A glass-walled, tilting rectangular flume which was 0.45-m wide, 0.45-m deep, and 19-m long was used. The bed slope was kept constant for all experiments, at 1%. Water was supplied to the flume using pumps that draw from a constant head reservoir. The temperature was kept constant at 21°C, using a cooling system within the reservoir. The flume was equipped with a 130-mm-high false floor within which a sediment recess was set. The 0.95-m-long recess was located 10.4 m downstream of the flume inlet. It extended the width of the flume and its depth was the full thickness of the false floor (Fig. 1). The sediment

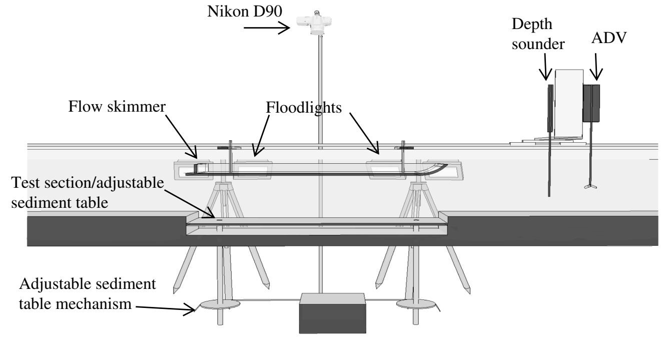

Fig. 1. Experimental setup

recess was filled with graded, rounded river gravels ranging from 0.15 to 27 mm in diameter and with density $\rho_s = 2{,}720\ \mathrm{kg/m^3}$. A large stone was placed in the center of the test section to stimulate cluster formation. A fixed bed with artificial roughness was installed on the false floor 2 m upstream of the recess. There was no sediment supply, and static armor conditions were achieved by the use of a vertically adjustable table, which formed the floor of the recess. The vertically adjustable table was monitored throughout each experiment, and it was slowly raised to ensure the upstream end of the test section was flush with the upstream false floor at all times.

To prevent disturbance of the bed, the flume was filled slowly to maximum depth, then the flow rate increased slowly while controlling the water level using an adjustable sharp-crested weir at the end of the flume. The flow rate was controlled using an orifice plate and was measured using a differential manometer. The calibration of the orifice plate was checked in situ using the laboratory calibration tanks that enable flow measurement to better than 1% accuracy. Additionally, using an acoustic Doppler velocimeter (ADV), a velocity profile was taken 1 m upstream of the test section at the center line of the flume to determine the flow characteristics. In a preparatory experiment, under the same experimental conditions, multiple velocity profiles were collected upstream and within the test section, and those confirmed that the flow was uniform and steady. The flow Reynolds number ($\mathsf{R} = \bar{u}H/v$, where H is the water depth, $\bar{u}$ is the depth-averaged streamwise velocity, and v is the kinematic viscosity) was 160×10^3 and the grain-size Reynolds number ($\mathsf{R}^* = u^* D_{50}/v$, where u^* is the shear velocity and D_{50} is the grain size at which 50% of the sample is finer) was 356, indicating fully turbulent flow. The time-averaged streamwise velocity profile of the flow was found to satisfy the logarithmic law. In the experimental setup, it was not possible to maintain the logarithmic velocity law while maintaining minimal side wall effects. As per Chin (1985), priority was given to maintaining the logarithmic velocity law, as this was used to determine shear velocities. Additionally, the formation of secondary flows, as they would occur in a natural gravel bed, was limited by the use of a straight-walled flume. Experiments were run at a constant flow rate for between 4 and 8 h, until static armor was achieved.

The experimental flow rates were selected to approach those under which the critical armor layer could form (Chin 1985). The critical shear stresses, τ_c, for entrainment were calculated (Petit 1994). D_{50} and D_{80} were 3.5 and 4.7 mm, respectively, and the shear stress at which critical armor layer is predicted, τ_{ca}, was 7.74 Pa (Chin 1985). The measured experimental shear stress τ was 6.35 Pa. The conditions supported the transport of all grain sizes and the formation of a static armor layer.

A total of 25 experiments were conducted as part of a wider look at cluster formation. As the focus of this paper is on individual

Table 1. Flow Conditions

Flow rate (Q) (l/s)	Water depth (h) (m)	Shear velocity (u^*) (m/s)	Reynolds number (R)	Froude number (F)	Shear Reynolds number [$R^*(D_{50})$]	Experiment duration (t) (min)
72	0.2	0.079	160×10^3	0.57	356	350

particle motion, a single experiment from the wider study is chosen for in-depth study. The flow properties of this experiment are presented in Table 1.

Sediment Preparation

Variation in the color of gravel-bed particles allowed motion detection. The sediment was separated into five size groups, with each group spray painted a different color (Table 2). Bright colors were chosen to contrast with one another. The gravel was manually mixed and placed into the test section of the flume so that it lay flush with the false floor. The same batch of gravel was used for all experiments, and sieve samples were taken regularly after experimentation to ensure that the grading curve was not altered due to loss of particles.

Camera Setup

A Nikon D90 DSLR camera with AF-S Nikkor 18-105 mm lens was positioned above the test section and remotely controlled through a computer. Still frames, at a resolution of $4{,}288 \times 2{,}848$ pixels, were taken at a rate of approximately 0.67 fps. The recording rate was restricted by the data transfer capabilities of software and hardware and allowed continuous recording of several hours. The recording rate was high enough to monitor the motion of larger particles in the test section. The images covered the full length (940 mm) and width (450 mm) of the test section. Images were resized to $750 \times 1{,}500$ pixels, which is essential for faster data processing and management. The smaller image size provided a minimum of approximately 200 pixels per white particle (the smallest particle that was tracked in the low-frequency images). This allowed the measurement of the angle of the long axis of white particles and the detection of small-scale movements. In the following discussion, those data are referred to as *low-frequency*.

A Casio EXILIM Pro EX-F digital camera was chosen to augment the low-frequency data with 30-fps data. While this frame rate and corresponding shutter speed allowed the clear motion capture of all the painted particles (coarser than D_{38}), it did not allow the clear motion capture of smaller grains due to hardware and lighting restrictions. In addition, the image resolution was not high enough to capture high-quality images of the entire bed, so a central section of the bed (approximately 200×350 mm^2) was recorded (Fig. 2). The resolution of this section of the bed ($720 \times 1{,}280$ pixels) provided a minimum of approximately 100 pixels per yellow particle (the minimum size of particle that was tracked). This was a suitable resolution to collect the position and basic dimensions of the particle; however, recording duration was limited to 20 min due to the FAT 32 4GB file size restriction. In the following discussion, those data are referred to as *high-frequency*.

To eliminate distortion of the image from reflection and refracting light caused by fluctuations of the water surface, a 1-m-long Perspex skimmer was placed over the test section. To minimize the effects of pressurization caused by having a constrained surface, the skimmer was adjusted to sit on the water at the level of the free surface.

Table 2. Sediment Grain Size Distribution and Coloring

Color	Percent finer (%)	Sieve size (mm)
Black	99.9	55
Red	98	25–27
White	80	9.5–25
Blue/green	55	4.5–9.5
Yellow	38	2.8–4.5
Natural (gray)	0	0.3–1.204

Digital Particle Tracking

An algorithm was developed to track sediment motion of the white and red particles (those greater than the D_{80}) in the low-frequency data sets. The low-frequency DPT algorithm was developed so that it does not rely on extremely small particle displacement between frames to operate. This enabled the monitoring of long-duration stochastic motion. The algorithm was also applied to high-frequency images and was used to detect all moving colored particles ($D > 2.8$ mm). Only transport events occurring on the surface layer of the bed could be captured using this method.

Particle-Tracking Algorithm

The Matlab Image Analysis Toolbox was used for all image processing and implementation of the DPT algorithm. Where barrel distortion of the image was greater than 2 mm (0.5% section width) at the test section boundary, a calibration algorithm was developed and applied to the experimental images to correct the distortion. The RGB intensity values for each pixel were observed, and the different color combinations for each colored fraction were determined using upper- and lower-threshold values and ratios between the three channels. This allowed analysis of individual-sized fractions, which provided a continuous quantification of the surface layer composition over the duration of this experiment.

The particle tracking process applied a two frame tracking algorithm based on image subtraction. (Blair and Dufresne 2005; Keshavarzy and Ball 1999; Radice et al. 2009). The following physical properties of the origin (a) and destination (b) of each moved particle were collected: x- and y-coordinates, plan area (A), particle orientation, and major and minor axis length.

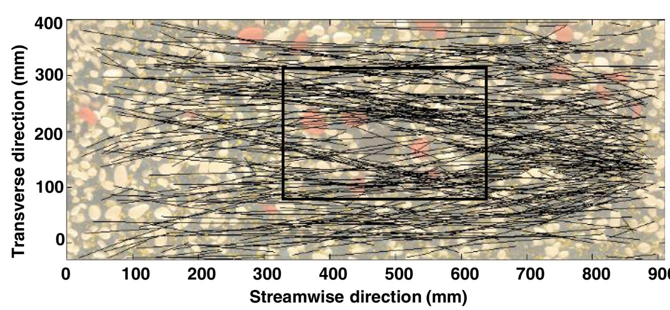

Fig. 2. Particle movements over the test duration (area of high-frequency data indicated in the box)

Linking the particle origin to the destination was achieved through the imposition of a number of thresholds. A survey of 90 particle movements within 60 frames was used to compile a set of threshold values, as follows:

- Forward movement only ($dx > 0$) was included.
- Displacement distance was less than the maximum specified ($dx < d\,\max$).
- y displacement was less than the maximum specified, decreasing as x displacement decreases until a minimum is reached, at which point the maximum y displacement was constant. This accounted for the rocking motion of particles ($dy < dy\,\max$).
- Particles were within the maximum and minimum specified size ($A\,\min < A < A\,\max$).
- The ratio between areas was less than the maximum specified ($Aa/Ab < A\mathrm{diff}\ \max$).

Particle pairs that conformed to these parameters then were given a compatibility weighting based on the following factors:

- Similarity of areas
- Similarity of major axis length
- Distance traveled
- Angle of direction of movement

Once all potential pairs were assessed, the pairs with the smallest weightings were assigned to one another as a *track.* Any particle in the image that left from the same position as that of the deposition of a previously tracked particle was assigned the same ID number as the tracked particle. The same algorithm was applied to the high-frequency images, with adjustment made to the threshold values of the algorithm.

In the analysis of the data, to eliminate all wobbling but not moving particles, only particles that were displaced a distance greater than one particle in diameter were included in the analysis (Drake et al. 1988; Wilcock and McArdell 1997).

Sediment Transport Rate Determination

Estimation of the sediment transport rate was obtained by summing the mass of all particles that were transported across a particular cross-sectional line, at a distance x along the bed. To calculate the volume ($\forall$), an assumption was made that the particle landed with its short axis vertical. On a rough surface, the effect of imbrication and hiding introduces errors into this assumption, which is the limiting factor. The mutually orthogonal dimensions of a sample of 100 grains were measured, giving the short axis, C, to be on average $0.5A$, the long axis. Using the volume of an ellipsoid, calculate the following equation:

$$\forall = \frac{4\pi abc}{3} \quad (1)$$

where a, b, and c are mutually perpendicular radii. Therefore, the volume of a sediment particle can be written as

$$\forall_{si} = \frac{\pi A_{si}^2 B_{si}}{12} \quad (2)$$

where the subscript si denotes *sediment* i and B denotes the medium-grain axis length. The sediment load is given by

$$q_{bx} = \frac{\rho_s}{\Delta t w} \sum \forall_{si} \quad (3)$$

where q_{bx} is the sediment transport rate in g/ms, Δt is the time step over which the sediment volume is summed, and w is the width of the test section.

Particle-Tracking Accuracy

The accuracy of the DPT algorithm was evaluated in a 100-frame sequence where all particle motion was manually recorded. The tracking accuracy was evaluated from two perspectives; the first test, termed *positive detection,* tallied the number of correct tracks divided by the total number of actual particle movements. The second test, termed *false detection,* tallied the number of particles assigned to incorrect locations divided by the number of total particle movements. The two tests measured different types of error in the algorithm: the first measured the percentage of fractional bedload motion that was detected by the algorithm, and the second measured the degree of error within the tracks that were detected. Therefore, the results of the two tests should not be added together. In the testing, 99% positive detection was achieved for the red particles (D_{98}), and 88% positive detection and 1.5% false detection was achieved for the white particles (D_{80}–D_{98}). Random accuracy checks were done frequently to ensure the suitability of the tracking thresholds for each experiment. Tracking accuracy was reduced for smaller sizes in the low-frequency data set due to their more dispersed nature and the 0.67 fps frame rate, which was too slow to capture a manageable number of particles.

For the high-frequency tracking, a 200-frame detailed survey was conducted to determine the tracking accuracy for each particle color. The white particles (D_{80}–D_{98}) were the most easily identifiable, with 98% positive tracking accuracy and 9% false tracks. The yellow particles (D_{38}–D_{55}) were also generally easily identifiable. However, due to their small size, at times they moved too fast to be clearly detected, therefore reducing tracking accuracy to 87%, with false detection of 8%. The green particles (D_{55}–D_{80}) were the most difficult to track because they were dark, and they were more difficult to detect against the background. They had 74% positive and 41% false detection. The red particles moved so infrequently that there was no opportunity to track them in the high-frequency data. The gray particles were not tracked.

Particle-Tracking Limitations

The accuracy results show that some incorrect matches were made in the DPT algorithm. Therefore, some outliers were expected. The threshold system within the algorithm means that it is common for an incorrect match of one particle to be made with another particle of similar physical and spatial properties; however, this is not always the case. The incorrect matches and any motion that is not detected introduced error into the results and are a likely source of statistical outliers.

In the high-frequency DPT, if a particle track was missed, the DPT algorithm would interpret the missed particle track as one particle landing and another being entrained. This had the effect of shortening the perceived entrainment distances and durations, but it had no effect on the instantaneous velocities and sediment transport rate quantification.

Physical measurement of the sediment transport rate was not undertaken in this study. The DPT algorithm detected only those particles that were both entrained and deposited within the test section, therefore eliminating any chance of detecting particles that moved from the test section farther downstream.

Results and Discussion

DPT algorithm results are shown in Figs. 2 and 3. Fig. 2 shows the track lines of all of the large particle movements ($D > 9.5$ mm) that occurred over the 350-min duration of the experiment. To reduce

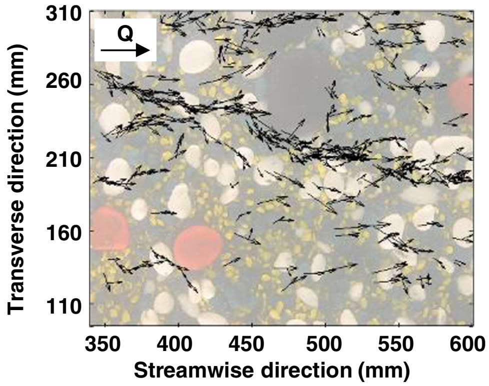

Fig. 3. Blue/green particle movements over 1 min; each arrow shows the position, direction, and relative velocity of a particle as it moves between frames

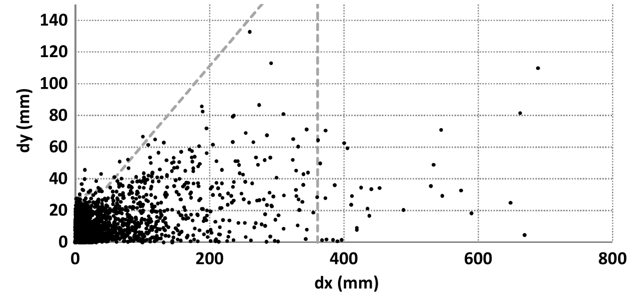

Fig. 4. Absolute streamwise and transverse distances traveled by particles for low-frequency data; dotted lines show the DPT distance thresholds applied to each frame

clutter, only the motion of particles that have moved completely outside of their previous position is shown. While the trajectories in Fig. 2 are straight lines, this is not necessarily the case, due to the low frame rate. The high-frequency DPT results are shown in Fig. 3. The black arrows represent the green particle velocities and directions that were detected on the bed over a 1-min time window. The location of the high-frequency recording area within the test section is shown in Fig. 2.

The DPT results were used to quantify the characteristics of particle motion as the bed was water-worked. The results from the low-frequency particle tracking provide limited information on the trajectory of entrained particles, but they enable the measurement of the sediment transport rate of this size fraction over the duration of the experiment, and allow investigation into the patterns of entrainment, displacement, and deposition that are so complex in a graded gravel bed. The high-frequency particle tracking complements the low-frequency results, in that it allows insight into particle trajectories. However, the duration of recording does not allow observation on timescales long enough to fully explore the development of complex bedforms.

Mode of Motion of Individual Particles

Because the DPT was applied from above the flume, no elevation data are available for the particle trajectories; therefore, only qualitative data are available on the mode of sediment motion. Bedload was the sole mode of transport, and the Rouse number ($z = v_s/\kappa u^*$ where v_s is the particle-settling velocity and κ is the von Karman constant) for the smallest particles was 2 and ranged up to 18 for the largest size. The mode of transport for the smallest particles was typically saltation, with rolling and sliding motion becoming more common as particle size increased. The white particle ($z = 11$) motion was primarily rolling, with some saltation observed. The red particles ($z = 18$) moved infrequently, with their mode of motion being either sliding or rolling. Drake et al. (1988) reported that essentially all particles larger than 7 mm rolled. The study observations of the saltation of particles larger than 9.5 mm indicate that this threshold is not absolute, and as the Rouse number implies, it also depends on the shear velocity.

Pathline of Bedload Particles

Fig. 4 shows the displacement vector measured from the point of entrainment to the point of disentrainment for each particle in motion in the low-frequency data series. The dashed lines indicate the distance thresholds applied to particle displacement between two frames, with numerous particles in motion for multiple frames. These displacements are the collation of the movements shown in Fig. 2. The mean streamwise displacement was 23 mm, (equivalent to 1–2.5 particle diameters), with a maximum displacement of 688 mm. The mean transverse displacement was 8.7 mm (equivalent to 0.5–0.9 particle diameters) with a maximum of 133 mm. Papanicolaou et al. (1999) measured similar mean streamwise displacements of 1.5–2.5 particle diameters, depending on the availability and density of particles on the bed.

The low-frequency data series did not capture the particle trajectory in detail; however, approximately 10% of all displaced particles were in motion for three or more consecutive images (3 s), allowing rudimentary evaluation of the sinuosity of these trajectories. *Sinuosity,* defined as the ratio of the curvilinear length to the straight-line distance traveled by a displaced particle, was measured for all yellow and white particle motion. Examples of particle displacement and the corresponding sinuosity values are shown in Fig. 5. The high-frequency images capture a detailed trajectory, but the sample size for white particles is small due to the limited number of large particle movements in the observation window. Probability distributions of the two sources of sinuosity data for the white particles, as well as the high-frequency sinuosity data from the yellow particles, are presented in Fig. 6. Both sources of data for white particles show that the sinuosity is closer to unity than that of smaller particles.

Observation of the bedload motion indicated particle sinuosity of the smaller particles arises from one of three sources. Either a low grain-to-bed-roughness ratio causes smaller particles to be diverted around larger particles, or particle trajectory is influenced by turbulent fluctuations or the secondary flow patterns generated by uneven bed surface. Larger particles are less susceptible to the transverse flow forces and when colliding with another large stone, they are more likely to simply stop or roll over the top (Drake et al. 1988), whereas small particles will be carried with the flow around the particle.

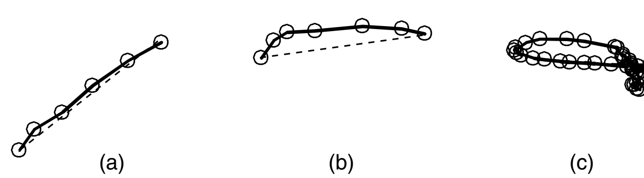

Fig. 5. Examples of particle sinuosity: (a) sinuosity = 1 [straight (a) sinuosity ≈ 1]; (b) sinuosity = 1.1; (c) sinuosity = 3.6

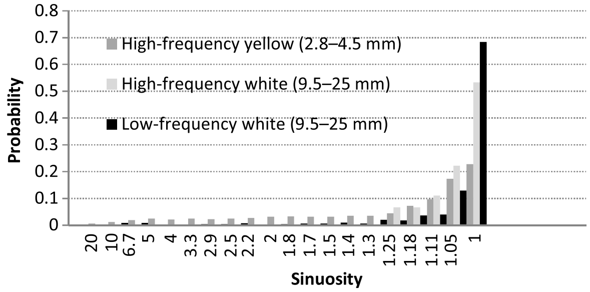

Fig. 6. Probability distribution of the sinuosity of individual particle movements for low-frequency and high-frequency particle motion

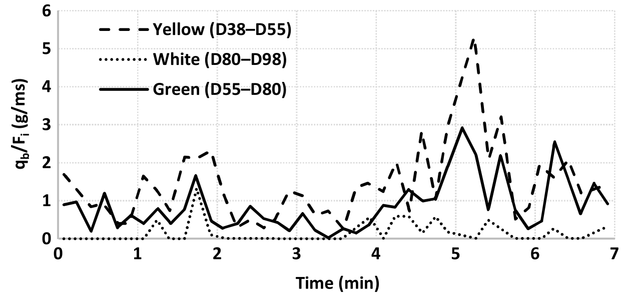

Fig. 9. Fractional sediment transport rate at $x = 550$ mm averaged every 10 s

Sediment Transport Rate

The sediment transport record of the experiment shows the development of the gravel bed toward a static armor. DPT enables spatiotemporal interrogation of the sediment motion, allowing the sediment transport rate to be measured at any point on the bed. A cross section, approximately midway along the length of the test section ($x = 630$ mm), was chosen. This position was far enough along the test section for the sediment transport rate to be fully developed, but not so close to the end of the section that entrained particles leaving the bed are not detected. The rates calculated were the average over each 60-s interval of the experiment duration. Fig. 7 shows that the initial sediment transport rate drops quickly within the first 20 min of the experiment. The high-frequency data were taken at 7 min, well within this period of high transport. The overall rate of transport fluctuates over the remaining 5 h.

The sediment transport rate from the high-frequency data can be separated into size fractions (Fig. 8). The values shown are the average over a 10-s window. The transport rate is generally higher for the smallest size (yellow particles), and lower for the largest size (white particles). Other fractional transport studies (Wilcock 1993; Wilcock and Crowe 2003; Wilcock and McArdell 1997) have scaled the transport rates by the percentage of bed surface comprised by that respective fraction. This allows evaluation of the sediment transport rate with reference to the available proportion of that sediment size (and therefore fraction entrainment probability). The fractional sediment transport rate, calculated using the surface fraction of each sediment size (5%, 15%, and 60% for yellow, green, and white stones, respectively) is presented in Fig. 9. This significantly changes the appearance of the transport record. Smaller particles are more frequently displaced for the majority of the observed period. The transport rate decreases with increasing grain size. Wilcock and McArdell (1993) observe that for smaller grains, the sediment transport rate is virtually independent of grain size, and transport is dependent only on the proportion of sediment available on the bed surface and the total transport rate. Finer division in the sediment fraction sizes would improve the detail that further investigation could reveal.

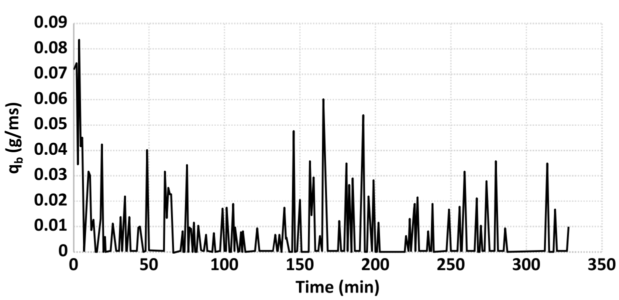

Fig. 7. Sediment transport rate of particles coarser than $D_{80} = 9.5$ mm

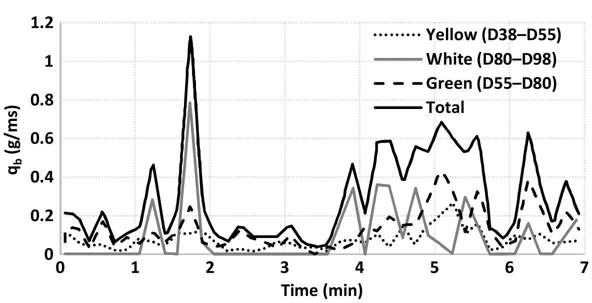

Fig. 8. Sediment transport rate at $x = 550$ mm, averaged every 10 s

Particle Movement Patterns

Previous studies have identified frequent, brief, localized, random sweep-transport events of high entrainment and transport (Drake et al. 1988; Papanicolaou et al. 1999). These events have been estimated to last between 1 and 2 s and are thought to be related to near-bed turbulence events. Localized events, such as those described by Drake et al. (1988), were also noticed in this study. Interrogation through the application of spatial and temporal limits on the high-frequency DPT results was conducted to isolate these events. Particle movements were digitally sorted by grouping entrainment that occurred temporally within 1/6 s of the previous movement and spatially within 10 mm in the transverse direction of the bed of the most recently entrained particle in the event. Fig. 10 shows an example of two isolated localized events, one starting

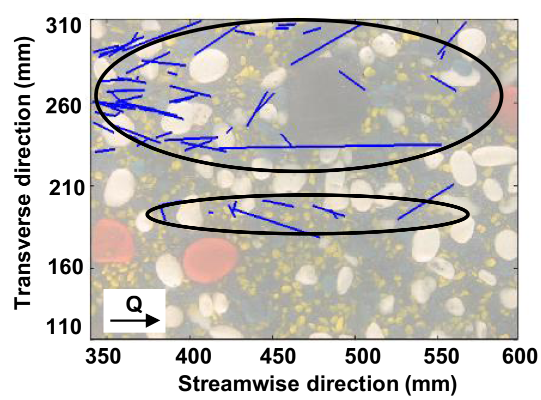

Fig. 10. Example of two localized entrainment events (each event circled) occurring over a 0.9-s period

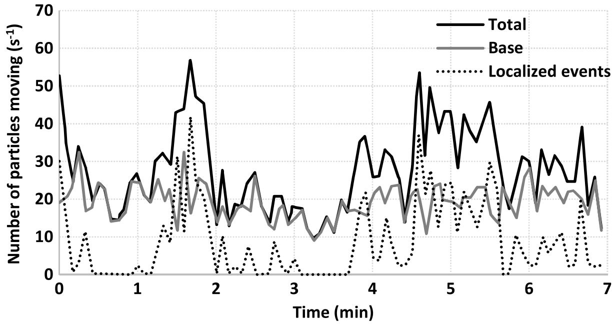

Fig. 11. Comparison of particles entrained in localized events, those not entrained in localized events, and the total entrained particles

from the upper-left corner of the frame, and the other stating from the center. For both events, the location of initial entrainment of particles moved downstream over time, which is exhibited in the figure by the elongated region of entrained sediment.

Approximately 30% of all particle movements that were recorded occurred as a part of a localized event, which is less than the 70% observed in field observations by Drake et al. (1988). Fig. 11 shows the rate at which particles are entrained in localized events over time. The number of particles entrained in localized events and the total number of particles entrained are compared. The relationship between the two values indicates that there may be a relatively constant baseline of particles that are entrained at a lower and constant rate. Accordingly, the particles entrained in the localized events are the major contributors toward fluctuation in the sediment transport rate.

Of the events that were identified, the maximum duration was less than 1 s, with the majority of events lasting less than 0.5 s. Longer event durations loosely correspond to higher numbers of entrained particles, with up to 80 particles entrained in a single event.

Velocity Distribution of Bedload Particles

Instantaneous flight velocities of particle motion were measured from the high-frequency data. The velocity of white and yellow particles was measured, while the velocity of green particles was not, due to higher uncertainty in the green DPT results. Streamwise (V_x), transverse (V_y), and tangential velocities (V_{xy}) were measured for the flight of each particle in motion between consecutive frames. An example of a particle trajectory, showing the flight velocity of the particle, is shown in Fig. 12. The graph is made up of several thousand measurements for the yellow particles and several hundred measurements for the white particles.

A probability density function (PDF) of the streamwise particle velocity was estimated (Fig. 13). The exponential relationship for

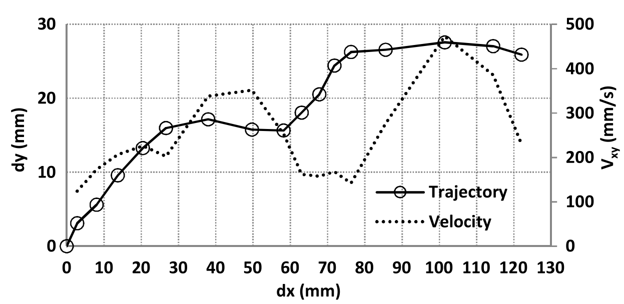

Fig. 12. Example of a particle trajectory showing the corresponding instantaneous particle velocity (V_{xy})

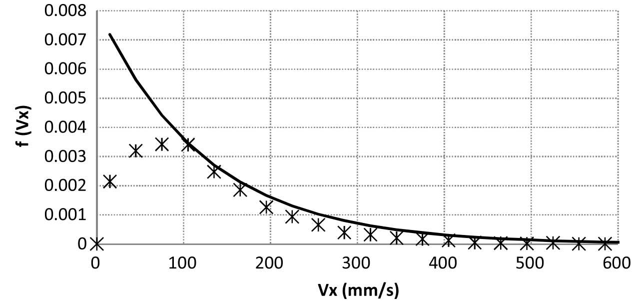

Fig. 13. PDF of V_x for the yellow ($D = 2.8$–4.5 mm) size fraction; crosses show experimental data, and the solid line shows the fit of data by Eq. (5); sediment motion was measured in the 7-min observation window of the high-frequency data

streamwise velocity, developed by Lajeunesse et al. (2010), was tested on these data:

$$P(V_x) = \frac{1}{V} e^{-V_x/V} \tag{4}$$

where V is the average streamwise particle velocity. The fit approximates the PDF relationship at the faster particle velocities well. The slower frame rate used in this study, compared to the 250-fps data of Lajeunesse et al. (2010), was not fast enough to capture the subtle changes at slower particle velocities, and Eq. (4) underrepresented those particle movements. QQ plots verified that the exponential relationship was the best fit for the data.

The relationship for the estimation of transverse velocity, proposed by Lajeunesse et al. (2010), was applied to the results from the present study (Fig. 14). The Gaussian function proposed by Lajeunesse et al. (2010) was modified to form a relationship that fit the data:

$$P(V_y) = \frac{1}{\pi\delta} e^{-(V_y/\delta)^2} \tag{5}$$

where δ is the standard deviation of the transverse velocity. The relationship shows good agreement with the experimental data.

The PDFs of the tangential velocity normalized by the grain size shear velocity (u_i^*) of the yellow particles are compared with those of the white particles in Fig. 15. The curves indicate that the white particles have a faster velocity than the yellow particles. This is contradictory to the observations of Drake et al. (1988), who found that larger particles were 30% slower than smaller particles on average, and proposed that the primary mode of motion for large particles was rolling, and hence they were often slowed by contact

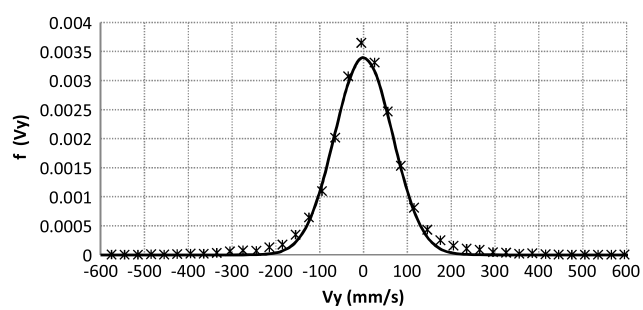

Fig. 14. PDF of V_y for the yellow ($D = 2.8$–4.5 mm) size fraction; crosses show experimental data, and the solid line shows the fit of data by Eq. (5); sediment motion was measured in the 7-min observation window of the high-frequency data

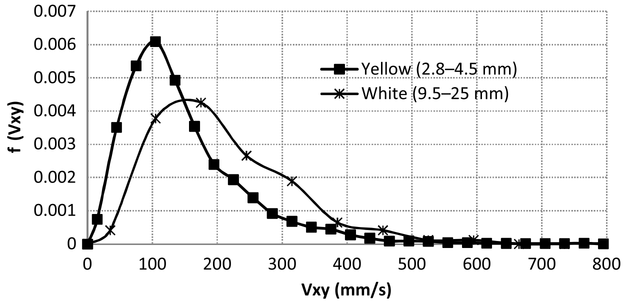

Fig. 15. Experimental PDF of V_{xy} for the yellow (2.8–4.5 mm) and white (9.5–25 mm) size fractions; sediment motion was measured in the 7-min observation window of the high-frequency data

with the bed, which explains their lower velocity. In the present study, a limited number of large particles move, most of these by saltation or rolling. The velocities of these movements are probably higher than the average velocity of the smaller particles. The numerous small particle movements include motion from all modes of transport, such that sliding and rolling particles will reduce the average velocity. Observation of the bed indicates that smaller particles are entrained by a wider range of flow conditions, including slower velocities than those that entrain the large particles.

Conclusions

Low-frequency (0.67-fps) and high-frequency (30-fps) experimental data of graded gravel sediment transport were obtained. The data cover continuous quantitative observation of the bed for up to the 8-h duration of the experiment. Intermittent high-frequency data were obtained to augment the low-frequency data, which allowed observation of detailed particle motion. The grains in the graded gravel bed were painted according to their size fraction. In this paper, a new DPT algorithm, developed for the application on graded gravels as they are water-worked, is presented and used to track the motion of grains larger than the D_{80} for low-frequency data, and to track all grains greater than the D_{38} for high-frequency data. Very high levels of accuracy were achieved when the algorithm was applied to the low-frequency data. When applied to the faster frame rate, the tracking algorithm produced varying levels of accuracy. High accuracy was achieved for larger or well-contrasting particles, and poorer accuracy was achieved for particles with dull contrast. Different aspects of sediment transport dynamics were investigated. Particle sinuosity was found to increase as particle size decreases. Fractional transport rates indicate that smaller particles are more frequently entrained for the majority of the observed period and the transport rate decreases with increasing grain size. The particle movement patterns identified by Drake et al. (1988) and Papanicolaou et al. (1999) have been quantified using image analysis. Approximately 30% of all particle movements that were recorded occurred as a part of a localized event. Instantaneous particle velocities indicate that the larger particles have a faster velocity than the smaller particles. This is contradictory to the observations of Drake et al. (1988), and the difference may arise from the different mode of motion of the particles that were observed.

Acknowledgments

The authors would like to thank four anonymous reviewers, whose comments helped to improve the manuscript.

Notation

The following symbols are used in this paper:

A, B, and C = mutually orthogonal dimension of a grain (m);
A_{si} = long axis of sediment i (m);
a, b, and c = mutually perpendicular radii (m);
B_{si} = medium axis of sediment i (m);
C_{si} = short axis of sediment i (m);
D = diameter (mm);
D_{50} = size of grain at which 50% of the sample is finer (mm);
D_{80} = size of grain at which 80% of the sample is finer (mm);
H = water depth (m);
q_{bx} = sediment transport rate (g/ms);
R^* = grain size Reynolds number;
R = flow Reynolds number;
t = time (s);
u^* = shear velocity (m/s);
$\bar{u}$ = depth averaged streamwise velocity (m/s);
u_i^* = *grain size* shear velocity (m/s);
V = velocity (m/s);
v = kinematic viscosity (m^2/s);
v_s = particle-settling velocity (m/s);
w = width (m);
z = Rouse number;
δ = standard deviation of the transverse velocity (m/s);
$\boldsymbol{\kappa}$ = von Karman constant;
ρ_s = density (kg/m^3);
τ_c = critical shear stress (pa);
τ_{ca} = shear stress at which critical armor layer is predicted (pa); and
$\forall$ = volume (m^3).

References

Ancey, C., Davison, A., Bohm, T., Jodeau, M., and Frey, P. (2008). "Entrainment and motion of coarse particles in a shallow water stream down a steep slope." *J. Fluid Mech.*, 595, 83–114.
Bathurst, J. C. (2007). "Effect of coarse surface layer on bed-load transport." *J. Hydraul. Eng.*, 10.1061/(ASCE)0733-9429(2007)133:11(1192), 1192–1205.
Biggs, B. J. F., Scarsbrook, M. R., Francoeur, S. N., and Duncan, M. J. (1997). "Bed sediment clusters: Are they the key to maintaining bio-diversity in New Zealand streams?" *Water Atmos.*, 5(1), 21–23.
Blair, D., and Dufresne, E. (2005). "Matlab particle tracking repository." ⟨http://physics.georgetown.edu/matlab/index.html⟩ (Sept. 5, 2009).
Böhm, T., Ancey, C., Frey, P., Reboud, J.-L., and Ducottet, C. (2004). "Fluctuations of the solid discharge of gravity-driven particle flows in a turbulent stream." *Phys. Rev. E*, 69(6), 061307.
Böhm, T., Frey, P., Ducottet, C., Ancey, C., Jodeau, M., and Reboud, J.-L. (2006). "Two-dimensional motion of a set of particles in a free surface flow with image processing." *Exp. Fluids*, 41(1), 1–11.
Buffington, J. M., Dietrich, W. E., and Kirchner, J. W. (1992). "Friction angle measurements on a naturally formed gravel streambed: Implications for critical boundary shear stress." *Water Resour. Res.*, 28(2), 411–425.
Buffington, J. M., and Montgomery, D. R. (1997). "A systematic analysis of eight decades of incipient motion studies, with special reference to gravel-bedded rivers." *Water Resour. Res.*, 33(8), 1993–2029.
Chin, C. O. (1985). "Stream bed armouring." Ph.D. thesis, Univ. of Auckland, New Zealand.
Drake, T. G., Shreve, R. L., Dietrich, W. E., Whiting, P. J., and Leopold, L. B. (1988). "Bedload transport of fine gravel observed by motion-picture photography." *J. Fluid Mech.*, 192, 193–217.

Dwivedi, A., Melville, B., and Shamseldin, A. Y. (2010). "Hydrodynamic forces generated on a spherical sediment particle during entrainment." *J. Hydraul. Eng.*, 10.1061/(ASCE)HY.1943-7900.0000247, 756–769.

Grass, A. (1971). "Structural features of turbulent flow over smooth and rough boundaries." *J. Fluid Mech.*, 50(2), 233–255.

Hassan, M. A., and Church, M. (2000). "Experiments on surface structure and partial sediment transport on a gravel bed." *Water Resour. Res.*, 36(7), 1885–1895.

Heays, K., Friedrich, H., and Melville, B. W. (2010). "Re-evaluation of image analysis for sedimentary process research." *Proc., IAHR APD Congress*, International Association for Hydro-Environment Engineering and Research, Asia Pacific Division.

Hergault, V., et al. (2010). "Image processing for the study of bedload transport of two-size spherical particles in a supercritical flow." *Exp. Fluids*, 49(5), 1095–1107.

Houssais, M., and Lajeunesse, E. (2012). "Bedload transport of a bimodal sediment bed." *J. Geophys. Res. Earth Surf.*, 117(F4), F04015.

Keshavarzy, A., and Ball, J. E. (1999). "Application of image processing in the study of sediment motion." *J. Hydraul. Res./De Recherches Hydrauliques*, 37(4), 559–576.

Komar, P. D. (1987). "Selective grain entrainment by a current from a bed of mixed sizes: A reanalysis." *J. Sediment. Res.*, 57(2), 203–211.

Lajeunesse, E., Malverti, L., and Charru, F. (2010). "Bed load transport in turbulent flow at the grain scale: Experiments and modeling." *J. Geophys. Res. Earth Surface*, 115(F4), F04001.

Lane, S. N., Chandler, J. H., and Porfiri, K. (2001). "Monitoring river channel and flume surfaces with digital photogrammetry." *J. Hydraul. Eng.*, 10.1061/(ASCE)0733-9429(2001)127:10(871), 871–877.

Nelson, J. M., Shreve, R. L., and Mclean, S. R. (1995). "Role of near-bed turbulence structure in bed load transport and bed form mechanics." *Water Resour. Res.*, 31(8), 2071–2086.

Papanicolaou, A. (1997). "The role of turbulence on initiation of sediment motion." Ph.D. thesis, Virginia Polytechnic Institute and State Univ., Blacksburg, VA.

Papanicolaou, A. N., Diplas, P., Balakrishnan, M., and Dancey, C. L. (1999). "Computer vision technique for tracking bed load movement." *J. Comput. Civ. Eng.*, 10.1061/(ASCE)0887-3801(1999)13:2(71), 71–79.

Parker, G., and Klingeman, P. C. (1982). "On why gravel bed streams are paved." *Water Resour. Res.*, 18(5), 1409–1423.

Petit, F. (1994). "Dimensionless critical shear stress evaluation from flume experiments using different gravel beds." *Earth Surf. Proc. Landforms*, 19(6), 565–576.

Pilotti, M., Menduni, G., and Castelli, E. (1997). "Monitoring the inception of sediment transport by image-processing techniques." *Exp. Fluids*, 23(3), 202–208.

Radice, A., Ballio, F., and Nikora, V. (2009). "On statistical properties of bed load sediment concentration." *Water Resour. Res.*, 45(6), W06501.

Radice, A., Malavasi, S., and Ballio, F. (2006). "Solid transport measurements through image processing." *Exp. Fluids*, 41(5), 721–734.

Radice, A., Nokes, R., and Ballio, F. (2010). "Preliminary results from an application of PTV to bed-load grains." *Proc., River Flow 2010*, IAHR-Fluvial Hydraulics, Technische Universität Braunschweig, Braunschweig, Germany.

Schuyler, A., and Papanicolaou, A. N. (2000). "Image analysis technique to track the evolution of sediment clusters." *Exp. Tech.*, 24(5), 31–34.

Wilcock, P. R. (1993). "Critical shear stress of natural sediments." *J. Hydraul. Eng.*, 10.1061/(ASCE)0733-9429(1993)119:4(491), 491–505.

Wilcock, P. R. (2001). "Toward a practical method for estimating sediment-transport rates in gravel-bed rivers." *Earth Surf. Proc. Landforms*, 26(13), 1395–1408.

Wilcock, P. R., and Crowe, J. C. (2003). "Surface-based transport model for mixed-size sediment." *J. Hydraul. Eng.*, 10.1061/(ASCE)0733-9429(2003)129:2(120), 120–128.

Wilcock, P. R., and McArdell, B. W. (1993). "Surface-based fractional transport rates: Mobilization thresholds and partial transport of a sand-gravel sediment." *Water Resour. Res.*, 29(4), 1297–1312.

Wilcock, P. R., and McArdell, B. W. (1997). "Partial transport of a sand/gravel sediment." *Water Resour. Res.*, 33(1), 235–245.

Wu, F. C., and Yang, K. H. (2004). "Entrainment probabilities of mixed-size sediment incorporating near-bed coherent flow structures." *J. Hydraul. Eng.*, 10.1061/(ASCE)0733-9429(2004)130:12(1187), 1187–1197.

Yalin, M. S. (1977). *Mechanics of sediment transport*, 2nd Ed., Pergamon Press, New York.

Yalin, M. S., and DaSilva, A. M. F. (2001). *Fluvial processes*, IAHR, Delft, the Netherlands.

Zimmermann, A. E., Church, M., and Hassan, M. A. (2008). "Video-based gravel transport measurements with a flume mounted light table." *Earth Surf. Proc. Landforms*, 33(14), 2285–2296.